González, Danilo; Sodupe Roure, Mariona; Rodríguez Santiago, Luis; [et al.]. «Surface morphology controls water dissociation on hydrated IrO2 nanoparticles». Nanoscale, Vol. 13, Issue 34 (September 2021), p. 14480-14489. DOI 10.1039/d1nr03592d

Surface morphology controls water dissociation on hydrated IrO_2 nanoparticles

Received 00th January 20xx,
Accepted 00th January 20xx

DOI: 10.1039/x0xx00000x

Danilo González,[a] Mariona Sodupe,[a] Luis Rodríguez-Santiago,[a] Xavier Solans-Monfort*,[a]

Iridium oxide is a highly efficient catalyst for the oxygen evolution reaction, whose large-scale application requires decreasing the metal content. This is achieved using small nanoparticles. The knowledge of the water-IrO_2 nanoparticle interface is of high importance to understand the IrO_2 behavior as electrocatalyst in aqueous solutions. In this contribution, DFT (PBE-D2) calculations and AIMD simulations on IrO_2 nanoparticle models of different sizes ($(IrO_2)_{33}$ and $(IrO_2)_{115}$) are performed. Results show that two key factors determine the H_2O adsorption energy and the preferred adsorption structure (molecular or dissociated water): metal coordination and hydrogen bonding with oxygen bridge atoms of the IrO_2 surface. Regarding metal coordination, and since the tetragonal distortion existing in IrO_2 is retained on the nanoparticle models, the adsorption at iridium axial vacant sites implies stronger Ir-H_2O interactions, which favors water dissociation. In contrast, Ir-H_2O interaction at equatorial vacant sites is weaker and thus the relative stability of molecular and dissociated forms become similar. Hydrogen bonding increases adsorption energy and favors water dissociation. Thus, tip and corner sites of the nanoparticle, with no oxygen bridge atoms nearby, exhibit the smallest adsorption energies and a preference for the molecular form. Overall, the presence of rather isolated tip and corner sites in the nanoparticle leads to lower adsorption energies and a smaller degree of water dissociation when compared with extended surfaces. .

Introduction

Iridium oxide (IrO_2) is a highly efficient catalyst for the oxygen evolution reaction (OER) in acidic media with high activity and stability[1–7] Moreover, it has been recently suggested as potential catalyst for other reactions such as converting light alkanes in value-added products.[8–10] Understanding its chemical properties is key for the further development of novel iridium oxide-based substances. This implies nanostructured materials with a high specific surface areas since the wide application of iridium-based materials suffers from the metal cost.[11–17] In this context, one can find a large list of examples where IrO_2 has been used in the form of nanoparticles of different sizes[16,18–29] including very small and narrowly distributed nanoparticles of less than 2 nm, which show outstanding catalytic activities for the OER reaction.[16,20,23,25,28]

A deep knowledge of the water-IrO_2 interface is required to further understand the IrO_2 behavior as electrocatalyst in aqueous solutions.[30] Thus, several authors have studied the water – IrO_2 interaction and water – IrO_2 interface.[31–33] Although the majority of the studies have focused on the most stable (110) surface, some of the most recent experimental and computational contributions on related MO_2 rutile-like materials outlined that the degree of water dissociation is orientation and material dependent.[34–36] Overall, IrO_2 shows adsorption energies between -211.5 and -152.9 kJ mol^{-1} and a degree of water dissociation of 100% on the most stable (110) surface, while this percentage decreases to around 60% in the (011) facet.[35]

Remarkably, despite the importance of IrO_2 nanoparticles, to the best of our knowledge, the effect of reducing the material dimensionality from films to nanoparticles in the H_2O – IrO_2 interface has not been addressed neither from experiments nor calculations. Nanoparticles either amorphous or crystalline are expected to present metal sites that are different from those found in extended surfaces, i.e. tip, corner and edges sites. Moreover, the nanoparticle shape can also play a role in favoring or decreasing the cooperative effects between adsorbed molecules. Indeed, this has recently been analyzed on H_2O-nanoparticle interfaces of related materials.[37,38] Therefore, it is likely that the local structure of the IrO_2 nanoparticle – H_2O interface is different from that of films. Indeed, contributions on related hydrated TiO_2 nanoparticles highlighted their differences with respect to crystalline facets and allowed to identify the distribution of OH groups over the surface as well as to analyze size effects.[37–41] In this contribution we focus on analyzing how the IrO_2 – H_2O interface varies when going from extended IrO_2 slabs to small Wulff-like nanoparticles. Results show that IrO_2 nanoparticle models are somewhat more ionic than extended surfaces and this favors the direct H_2O-metal interaction. However, the convex shape of the nanoparticle prevents the formation of strong hydrogen bonds either between the surface or adjacent adsorbed molecules. Moreover, the number of accessible oxygen bridge that assist water dissociation is more limited. Overall, these two factors

---

[a] Departament de Química, Universitat Autònoma de Barcelona, 08193 Bellaterra, Spain

Electronic Supplementary Information (ESI) available: [details of any supplementary information available should be included here]. See DOI: 10.1039/x0xx00000x

decrease the degree of dissociated water molecules on the surface of the nanoparticle with respect to thin films and leads to lower adsorption energies per water molecule, particularly at the most accessible corner and tip sites.

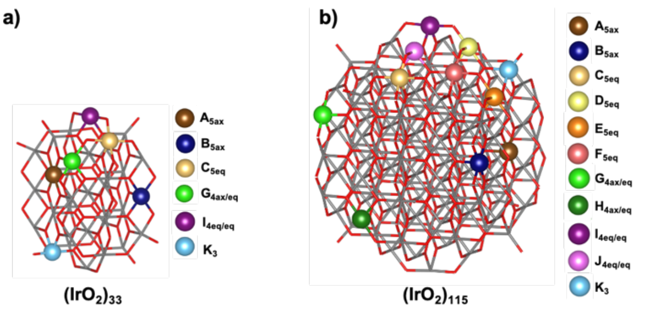

Figure 1. (a) $(IrO_2)_{33}$ and (b) $(IrO_2)_{115}$ nanoparticle models with the different undercoordinated iridium centers (colored atoms).

Computational details

Models

We use a four-layers thick slab to represent the main crystallographic surfaces. A (2x2) supercell was considered for each facet to avoid lateral interactions with neighbor images. These models are equivalent to those used in our group for modeling RuO_2, TiO_2 and IrO_2 surfaces.[34,35,42] For the nanoparticles we use two stoichiometric models of 1.2 and 1.8 nm large constructed with BCN-M, a python-based computational tool able to construct Wulff-like nanoparticle models (Figure 1).[43] For that, we considered the surface energies of the four most representative families of IrO_2 facets ({110}, {100}, {011} and {001}) computed in our previous work (0.150, 0.158, 0.185 and 0.206 eV A^{-2} for (110), (011), (100) and (001), respectively).[35] The initial models contain 33 and 115 IrO_2 units, respectively, and arise from cutting the bulk, thus the geometry around undercoordinated metal centers is far from optimal and a further geometry optimization accounting for the surface relaxation is performed. Optimization in vacuum implies reorganization around the nanoparticle tip with the formation of Ir-Ir bonds. This reorganization does not occur when a water monolayer is added on the nanoparticle surface (See details in the Electronic Supplementary Information (ESI)). Since IrO_2 nanoparticle are usually synthetized in aqueous solution, optimization in the presence of water is more realistic. Therefore, we decided to perform constrained optimizations of $(IrO_2)_{33}$ and $(IrO_2)_{115}$ nanoparticle models taking the geometries of the optimized $(IrO_2)_{33}$•$38H_2O$ and $(IrO_2)_{115}$•$88H_2O$ nanoparticle monolayer systems, respectively, that includes one water molecule per iridium vacant site. In the constrained optimizations, the nanoparticle is frozen and only water molecules and the singly coordinated oxygen atoms are allowed to relax. Analysis of the different unsaturated metal centers after removing the water molecules reveal that there are eleven and six different sites for the $(IrO_2)_{115}$ and $(IrO_2)_{33}$ nanoparticles respectively (Figure 1). The existing sites can be divided in five groups: i) pentacoordinated centers with an axial vacant site ($\mathbf{A_{5ax}}$ and $\mathbf{B_{5ax}}$); ii) pentacoordinated centers with an equatorial vacant site ($\mathbf{C_{5eq}}$, $\mathbf{D_{5eq}}$, $\mathbf{E_{5eq}}$ and $\mathbf{F_{5eq}}$); iii) tetracoordinated centers with one axial and one equatorial vacant site ($\mathbf{G_{4ax/eq}}$ and $\mathbf{H_{4ax/eq}}$); iv) tetracoordinated centers with two equatorial vacant sites ($\mathbf{I_{4eq/eq}}$ and $\mathbf{J_{4ax/eq}}$); and v) metal centers presenting only three bonds with lattice oxygens ($\mathbf{K_3}$).

Level of theory

The electronic structure of $(IrO_2)_N$ and the water adsorption energies to these nanoparticle models are studied with the VASP package[44,45] which uses periodic DFT calculations in the three dimensions. Consequently, calculations are performed by considering a 30 and a 35 Å edge large cubic box for $(IrO_2)_{33}$ and $(IrO_2)_{115}$, respectively. This ensures at least 18 Å between images. We used PBE density functional[46] with Grimme's D2 empirical correction[47] to account for dispersion forces. The effect of the dispersion correction was analyzed by performing test calculations on sites $\mathbf{G_{4ax/eq}}$ and $\mathbf{I_{4eq/eq}}$ of the $(IrO_2)_{33}$ nanoparticle with PBE-D3. Results are reported in Table S1 and show that PBE-D2 and PBE-D3 leads to equivalent results. The ionic cores were described with PAW pseudopotentials[48,49] and the valence electrons were represented with a plane-wave basis set with an energy cutoff of 500 eV. All calculations were performed at gamma point. This methodology is equivalent to the one we used for describing the water adsorption on the different crystallographic facets of RuO_2[34] and for studying the OER activity on IrO_2 surfaces[42] and on isolated iridium atoms supported on iridium tin oxide.[15] In the three cases, the computational data reproduced the experimental evidences,[15,36,50] indicating that the computational protocol is accurate enough for reproducing main trends on these materials.

Thermal effects at 1 atm and different temperatures were taken into account for the adsorption of two water molecules at the $\mathbf{G_{4ax/eq}}$ and $\mathbf{I_{4eq/eq}}$ sites of the $(IrO_2)_{33}$ nanoparticle. Only the vibrational contributions of the normal modes associated with the adsorbed species (H_2O or OH^-/H^+) were considered. Table S3 shows the relative stabilities of the different forms at four different temperatures, the values suggesting a small influence of the temperature in favoring either the molecular or dissociated forms.

We also performed spin-polarized calculations with the aim of analyzing if reducing the material size has an effect on its magnetic properties. The results with the spin-polarized formalism are reported in the Electronic Supplementary Information and show that water adsorption is only marginally affected by the magnetism of the nanoparticle and more importantly, the same preference for the molecular or dissociated form is found for each site when using spin- or non-spin polarized calculations. Thus, the values reported in the main text are all obtained with the non-spin polarized formalism.

With the aim of exploring the different water – MO_2 interface at high coverages, we also performed ab-initio molecular dynamics at 300 K of the $(IrO_2)_{33}$•$38H_2O$ monolayer in the NVT ensemble. These simulations were performed at the same level of theory as that of geometry optimizations. Each simulation is

10 ps large and the analysis was performed on the last 5 ps. The time step size was fixed to 1 fs. During the AIMD simulations only the singly coordinated atoms of the nanoparticle model and the water molecules were allowed to move.

Electronic structure analysis is performed by computing the iridium d- and oxygen p-orbital band centers of the projected density of states (PDOS) as defined previously:[51–53]

$$\varepsilon_{Ir,O} = \frac{\int_{\varepsilon_{min}}^{\varepsilon_{max}} \varepsilon\rho(\varepsilon)d\epsilon}{\int_{\varepsilon_{min}}^{\varepsilon_{max}} \rho(\varepsilon)d\epsilon} \qquad (1)$$

Where $\varepsilon_{Ir,O}$ is the band center, ε is the energy with respect to the Fermi level and $\rho(\varepsilon)$ is the PDOS. In our case, the ε_{min} and ε_{max} values are set to -10 and 5eV around the Fermi level, respectively.

Results and discussion

We organized the results and discussion section in four parts. First, we describe the intrinsic adsorption of one water molecule on the main crystallographic facets of IrO_2. In a second step, we analyze the metal – water interaction at the different sites of the $(IrO_2)_{33}$ Wulff like nanoparticle (Figure 1). In the third part, we describe the effect of increasing the nanoparticle size. Finally, we discuss the cooperative and thermal effects on the smallest nanoparticle by modeling a water monolayer coverage, formed by adding one water molecule per vacant site (38 water molecules on $(IrO_2)_{33}$).

Intrinsic water – IrO_2 main crystallographic facets interaction.

The iridium centers present a distorted octahedral coordination characterized by a tetragonal compression with two short axial distances and four long equatorial ones, thus leading to two types of vacant sites for the iridium centers on the surface. The adsorption of water on IrO_2 occurs on these undercoordinated iridium atoms. The Ir-H_2O adsorption implies charge transfer from H_2O to iridium. This increases the acidity of water and thus, it favors water dissociation by transferring a proton to an oxygen bridge atom of the surface. Indeed, two conformations are plausible: the molecular (**mol**) and dissociated (**dis**) forms and their relative stability mainly depends on the iridium-H_2O interaction and the basicity of the oxygen bridge. Table 1 reports the H_2O adsorption energies on the four surfaces, the main geometrical parameters, and the iridium d- and oxygen p-DOS band centers. The H_2O adsorption energies range between -211.5 and -146.0 kJ mol^{-1}. The highest adsorption energy is computed for the (110) surface, while the weakest interaction takes place between water and the iridium centers of the (011) facet.

The undercoordinated iridium centers on the main crystallographic surfaces present three different coordination environments and the observed trends can be understood according to the metal coordination. The (110) and (100) surface present pentacoordinated unsaturated centers with the vacant site in axial position. Since Ir-O_{ax} distances are shorter than the equatorial ones, the Ir-H_2O interaction in these (110) and (100) surfaces are high and thus, there is a preference for the **dis** form. On the other side, the (011) surface has pentacoordinated iridium centers with the vacant site in an equatorial position. Consequently, the interaction is weaker than in the two previous surfaces and the **mol** form is preferred. Finally, the (001) surface presents tetracoordinated centers with two equatorial vacant sites. Therefore, the metals on this surface are the most undercoordinated centers and the adsorption of the first water molecule is strong, with the **dis** form being lower in energy by 1.4 kJ mol^{-1}. The adsorption of a second water molecule is not such favorable. The metal center is less electron deficient after the adsorption of the first water molecule and thus the mean adsorption energy per water molecule decreases significantly. Overall, the preferred structure on the (001) surface present two non-dissociated water molecules in line with the weak adsorption energy for the coordination to an equatorial site.

Table 1. H_2O adsorption energies on the main crystallographic surfaces (in kJ mol^{-1}), Ir-O and H···O hydrogen bond distances (in Å) and Iridium d orbital (ε_{Ir}) and oxygen p orbital (ε_O) band centers of the atoms involved in the adsorption and potential dissociation.

Site		E_{ads}	Ir-O	O···H	ε_{Ir}	ε_O
(110)	Dis	-211.5	1.970	2.043	-2.2	-2.5
(100)	mol	-191.2	2.074	1.683	-2.5	-3.0
	Dis	-193.1	1.960	1.688		
(011)	mol	-153.0	2.108	1.549	-2.9	-3.7
	Dis	-146.0	2.025	1.372		
(001)	mol	-201.7	2.086	1.591	-3.0	-3.3
	Dis	-203.1	1.982	1.632		
Site		E_{ads}	Ir-O	Ir-O	e_{Ir}	e_O
(001)-2H_2O	mol/mol	-183.1	2.099	2.098	-3.0	-3.3
	dis/mol	-177.4	1.991	2.103		
	dis/dis	-175.5	1.983	2.036		

The differences in adsorption energies can also be rationalized by analyzing the projected density of states (DOS) of the surface iridium d and oxygen p orbitals and, particularly the band center (ε) of each type of orbitals (Table 1 and Figure S3 of the ESI). According to previous contributions, iridium d-band centers close to the Fermi Level (less negative) lead to stronger metal-adsorbate interactions,[51–53] since in the case of metal oxides this is indicative of the presence of antibonding empty states[51] that accept the electron density from the adsorbate. The d-band center of unsaturated metals with axial vacant sites ((110) and (100) surfaces) have less negative values than those of the (011) and (001) surfaces. Therefore, the Ir-H_2O interaction is higher in the formers than in the latters. Moreover, the center of the p-oxygen band can also be used to determine the basicity of the oxygen bridge: the closer to the Fermi level the p band center is, the closer to the Fermi level the doubly occupied p orbitals of oxygen bridge are and thus, the higher basic character these oxygen atoms have. Accordingly, the O_{br} basicity trend is (110) > (100) > (001) > (011) and this agrees with the higher adsorption energy and the larger preference for the dissociated form at the (110) surface when compared to the (100) one, the two surfaces with axial vacant sites.

Water – $(IrO_2)_{33}$ nanoparticle interaction.

Results for the single H_2O-$(IrO_2)_{33}$ nanoparticle interaction are described site per site starting from the most saturated centres. When possible, relation with similar undercoordinated iridium centres of the main crystallographic surfaces is made. Table 2 presents the adsorption energies and the iridium d and oxygen p DOS band centres and Figure 2 shows the most relevant optimized geometries (other structures are in the ESI).

$A5_{ax}$, **B_{5ax}** and **C_{5eq}** are pentacoordinated iridium centres. **A_{5ax}** corresponds to an undercoordinated metal on the (110) surface of the nanoparticle with an axial vacant site. The adsorption of a water molecule in this **A_{5ax}** site implies water dissociation, with a formal Ir-OH- fragment and a protonated oxygen bridge of the edge. All attempts to find the **mol** form evolved spontaneously to dissociated water as in the case of the (110) surface. The Ir-O distance (1.990 Å) is slightly shorter than that computed for the (110) surface (2.018 Å). Moreover, the transferred proton and the Ir-OH fragment interact through a strong hydrogen bond with a short O···H distance (1.774 Å). These geometrical features agree with a slightly higher adsorption energy at the nanoparticle than on the (110) surface (-229.8 vs. -211.5 kJ mol^{-1} for **A_{5ax}** and (110), respectively). Therefore, site **A_{5ax}** behaves similarly to the (110) surface with a small increase on the adsorption energy.

The **B_{5ax}** site is located at the edge defined by two {110} surfaces and presents an axial vacant site. The water adsorbed at **B_{5ax}** dissociates, similarly to what has been described for **A_{5ax}**, and this leads to Ir-OH$^-$ and a protonated oxygen bridge at the (110) surface. The Ir-O distance (1.984 Å) and the adsorption energy (-225.5 kJ mol^{-1}) are similar to the value found for **A_{5ax}**. That is, **A_{5ax}** and **B_{5ax}** share the same vacant site and flat morphology around the site, thus water adsorption is similar.

Table 2. H_2O adsorption energies on $(IrO_2)_{33}$ sites in kJ mol^{-1} and Iridium d orbital (ε_{Ir}) and oxygen p orbital (ε_O) band centers of the atoms involved in the adsorption and potential dissociation.

Site	E_{mol}		E_{dis}		ε_{Ir}	ε_O
A_{5ax}	--[a]		-232.6		-2.6	-2.2
B_{5ax}	--[a]		-229.2		-2.8	-2.1
C_{5eq}	-138.2		-153.0		-2.6	-2.4
$G_{4ax/eq}$	-172.3		-189.2		-2.1	-2.7/3.3[b]
$I_{4eq/eq}$	-181.0		-187.1		-2.2	-3.2[b]
K_3	--[a]		-192.9			
	$E_{mol/mol}$	$E_{dis/mol}$	$E_{mol/dis}$	$E_{dis/dis}$		
$G_{4ax/eq}$	-160.2	-167.8	-159.0	-165.7	-2.1	-2.7/3.3[b]
$I_{4eq/eq}$	-163.6	-162.6	-162.2	N.A.	-1.8	-3.2[b]
K_3	--[a]	--[a]	--[a]	-163.7		

[a] All attempts to find the **mol** form evolved to the **diss** one; [b] Values corresponding to the dangling oxygen, which is well-placed for stablishing H-bonding interactions with the adsorbed H_2O molecule.

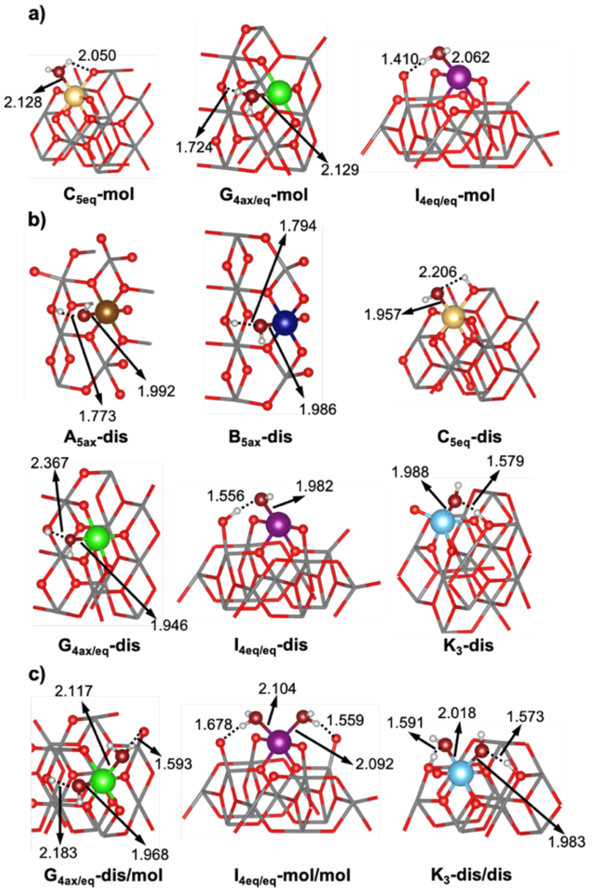

Figure 2. Optimized structure for the molecular (a) and dissociated (b) water adsorption at the different $(IrO_2)_{33}$ nanoparticle sites. (c) Most stable structure for the adsorption of two water molecules in tetracoordinated iridium surface centers. See Figure 1 for labelling. Distances are in Å

C_{5eq} is located at a corner formed by two {011} and one {110} facets. The iridium centre at this site has an equatorial vacant site similarly to those of the (011) surface. The adsorption of a water molecule at **C_{5eq}** can take place both in the molecular and dissociated forms, as on the (011) facet. However, at variance to the (011) surface, the dissociated form is preferred over the molecular one and this is indicative of a stronger Ir···O_W interaction. In any case, the adsorption energies (-133.6 and -148.7 kJ mol^{-1} for the **mol** and **dis** forms, respectively) are lower than those computed for the (011) extended surface, which can be explained by the convex environment around **C_{5eq}** that prevents the formation of hydrogen bonds with nanoparticle surface oxygen bridge atoms. Overall, while the preference for the dissociated form suggests a stronger Ir-H_2O interaction that increases water acidity, the absence of hydrogen bonding, globally leads to weaker adsorption energies.

$G_{4ax/eq}$ and **$I_{4eq/eq}$** sites are tetracoordinated. **$G_{4ax/eq}$** is placed at a corner defined by two {110} and one {011} facets, it has one axial and one equatorial vacant sites and thus, has no analogy with any of the surface models. **$I4_{eq/eq}$** is located at the tip of the nanoparticle, has two equatorial vacant sites and resembles the undercoordinated centres of the (001) extended surfaces. Adsorption of the first water molecule to these tetracoordinated sites is quite strong as found for the (001) extended surface. Therefore, although the two potential conformations exist (**mol** and **dis**), the dissociated form is preferred in both cases. Since **$G_{4ax/eq}$** has one axial vacancy, the adsorption of the first water molecule is stronger and the preference for the dissociation form higher in **G$_{4ax/eq}$** than in **I$_{4eq/eq}$**. Similar to **C$_{5eq}$**, the convex nanoparticle morphology around these sites makes the hydrogen bond less efficient and this leads to final adsorption energies that are smaller than the adsorption of one water molecule on the (001) surface as well as the face and edge sites of the nanoparticle, although the geometrical parameters suggest that the intrinsic Ir-H_2O interaction at these sites may be marginally higher than on a surface model.

The adsorption of a second water molecule in these two sites is less favourable than the adsorption of the first water molecule and this makes that the adsorption energy per water molecule decreases significantly. The weaker Ir-H_2O interaction when two water molecules are present favours the **mol** forms. In the case of **I$_{4eq/eq}$**, the most favourable structure is **mol/mol** as already found on the (001). In contrast, the preferred structure for the adsorption of two water molecules at **G$_{4ax/eq}$** has a molecular water at the equatorial site and a dissociated water at the axial site (**dis/mol**). This agrees with the global trend that indicates a clear preference for the dissociated form at axial sites, while the two structures co-exist in the equatorial ones. Remarkably, due to the intrinsic stronger Ir···H_2O interaction at the 1.2 nm nanoparticle model when compared with analogous extended surfaces, the energy difference between the molecular and dissociated forms of water adsorbed in equatorial sites is small both at **G$_{4ax/eq}$** and **I$_{4eq/eq}$** and, indeed, it is significantly smaller than the energy difference computed at the (011) surface.

Similarly to **I$_{4eq/eq}$**, **K$_3$** has two equatorial vacant sites and thus one would expect some analogies on the water adsorption at the two sites. Nevertheless, **K$_3$** is linked to the nanoparticle through only three Ir-O bonds and the sixth position is occupied by a singly coordinated oxygen, that shows a short Ir-O distance. This different coordination environment and the morphology of the nanoparticle around **K$_3$** site influence significantly the water adsorption. In particular, the adsorption of one water molecule at **K$_3$** takes place through water dissociation and all our trials to obtain a structure with molecular water evolved to the same dissociated form. This suggest that the preference for the dissociated form is higher than in the other tetracoordinated sites. Moreover, the transferred proton binds to an oxygen bridge that is more basic (see ε_O in Table 2) than the dangling involved in the H^+ transfer at **I$_{4eq/eq}$** allowing the formation of a hydrogen bond which strengthens the interaction between the adsorbed species and the surface. The higher intrinsic Ir-H_2O interaction at **K$_3$** when compared to **I$_{4eq/eq}$** and the additional stabilization through hydrogen bonding at the former site only, lead to a higher adsorption energy that is close to that obtained at **A$_{5ax}$** and **B$_{5ax}$** sites. Moreover, although the adsorption of the second water molecule is weaker as in the case of the other tetracoordinated sites, the preferred form for the adsorption of two water molecules at **K$_3$** is the **dis/dis**. All these data indicates that the presence of the dangling oxygen atom favours water adsorption with respect to similar sites.

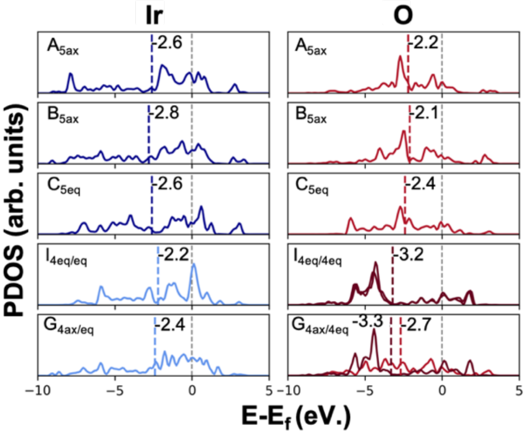

Figure 3. Projected Density of States (PDOS) and the associated band centers of the iridium d- and oxygen p-orbitals of the atoms involved in the H_2O adsorption at the different $(IrO_2)_{33}$ nanoparticle sites.

Analysis of the projected density of states of the d orbitals of iridium centres defining each site and the p orbitals of the oxygen bridge able to form hydrogen bonds gives additional insights on the preference for the dissociated or molecular forms as well as on the intrinsic Ir-H_2O interaction (Figure 3). Comparison of the band centres for the extended surfaces (Table 1) and those for the different sites of the nanoparticle (Table 2) reveals that both the band centre of the iridium d orbitals and the band centre of the oxygen p orbitals are closer to the Fermi level and consequently the intrinsic Ir-H_2O interaction is stronger, and the dissociation feasibility increased. Although this analysis could be influenced by the fact that we are performing constrained optimizations, IrO_2 at the 1.2 nm nanoparticle model appears to be more ionic than on extended surfaces, thus increasing metal acidity and oxygen basicity. Particularly, the oxygen atoms that can be involved in the water dissociation at site **I$_{4eq/eq}$** are the least basic (dangling oxygen), and thus, **I$_{4eq/eq}$** is the only site where the most stable structure has only molecular water.

Overall, the analysis of the adsorption of one water molecule on the 10 sites analyzed so far (four surfaces and six nanoparticle sites) suggests that the metal coordination and nature of the vacant site has an important role in determining the preferred structure of water upon adsorption (**dis** form at the axial ones and competition between **mol** and **dis** forms in the equatorial sites). Size reduction increases the ionicity of IrO_2, which favors both the intrinsic Ir-H_2O interaction and water dissociation. The final adsorption energy is also controlled by the hydrogen bonding between the adsorbed water and the material surface, and this is strongly influenced by the location of the undercoordinated metal center. The convex morphology around iridium centers located at corner and tip sites of the nanoparticle makes hydrogen bonding less efficient, thus leading to weaker interactions in these sites.

Influence of the nanoparticle size in H_2O adsorption: H_2O-$(IrO_2)_{115}$.

With the aim of analyzing how the nanoparticle size tunes IrO_2 ionicity and the feasibility of hydrogen bonding, we considered the adsorption of one water molecule per vacant site in the 11 different positions of the $(IrO_2)_{115}$ nanoparticle model (Figure 1). The eleven sites are divided in the same five group as before

(Figure 1). For each site, we considered those structures that were found as minima on the $(IrO_2)_{33}$ nanoparticle. Table 3 reports the H_2O adsorption energies and the iridium d- and oxygen p-DOS band centers and Figure 4 shows the optimized structures of the preferred forms in each site. All other structures can be found in the Electronic Supplementary Information.

Table 3. H_2O adsorption energies on $(IrO_2)_{115}$ sites in kJ mol^{-1} and Iridium d orbital (ε_{Ir}) and oxygen p orbital (ε_O) band centers of the atoms involved in the adsorption and potential dissociation.

Site	E_{mol}		E_{dis}		ε_{Ir}	ε_O
A_{5ax}	--[a]		-231.3		-2.2	-1.8
B_{5ax}	--[a]		-218.6		-2.2	-1.9
C_{5eq}	-111.9		-64.0		-2.0	-3.4
D_{5eq}	-134.3		-84.9		-2.4	-3.3
E_{5eq}	-140.6		-168.0		-2.0	-2.6
F_{5eq}	-108.5		-183.3		-2.3	-2.5
	$E_{mol/mol}$	$E_{dis/mol}$	$E_{mol/dis}$	$E_{dis/dis}$		
$G_{4ax/eq}$	-151.6	-155.7	--[b]	--[b]	-2.1	-2.5/--[e]
$H_{4ax/eq}$	--[c]	-190.6	--[b]	-212.2	-2.1	-2.5/-1.8
$I_{4eq/eq}$	-113.8	--[b]	--[b]	--[b]	-2.3	--[e]/--[e]
$J_{4eq/eq}$	--[d]	-182.6	--[b]	--[d]	-2.3	-2.7
K_3	--[b]	--[b]	--[b]	--[b]	-2.4	-2.4

[a] Attempts to find the **mol** form evolved to the dis one; [b] Not computed structure; [c] Attempts to find the **mol/mol** form evolved to the **dis/mol** one; [d] Attempts to find this structure evolved to the **dis/mol** form; [e] There are not unsaturated oxygen atoms close to this vacant site.

The adsorption energies on the different sites of the $(IrO_2)_{115}$ nanoparticle model range from -231.3 to -111.9 kJ mol^{-1}. These values are similar to those computed for the smaller model and the same general trends observed for the $(IrO_2)_{33}$ nanoparticle are also found for $(IrO_2)_{115}$. H_2O adsorbed on metal axial vacant sites dissociates leading to an OH^-/H^+ structure in which a nearby oxygen bridge is protonated and this is regardless site position and coordination (penta- or tetracoordinated). In contrast, the two structures are usually found for the equatorial vacant sites and the preferred form is highly related with the feasibility of forming a strong hydrogen bond that favors dissociation. That is, since hydrogen bonding in the **dis** form tends to be stronger than in the **mol** structure, the presence of a nearby oxygen bridge favors water dissociation. Moreover, the nanoparticle morphology around the site determines the formation/absence of hydrogen bonding and thus the final adsorption energy.

In this context, H_2O adsorption at $\mathbf{A_{5ax}}$ and $\mathbf{B_{5ax}}$ occurs through the dissociated form, presents strong hydrogen bonding and high adsorption energies. Indeed, the final computed values are in between those of the equivalent sites in the $(IrO_2)_{33}$ nanoparticle model and the (110) slab, which presents the same type of iridium coordination. Similarly, the adsorption at $\mathbf{H_{4ax/eq}}$ and $\mathbf{G_{4ax/eq}}$ always implies a dissociated water molecule in the axial position (as in the $(IrO_2)_{33}$ nanoparticle model). However, the preferred form for the equatorial position is **dis** in $\mathbf{H_{4ax/eq}}$ and **mol** in $\mathbf{G_{4ax/eq}}$. $\mathbf{H_{4ax/eq}}$ presents a well-suited oxygen bridge able to interact through hydrogen bonding with the water molecule in equatorial position and this promotes water dissociation and leads to a high mean adsorption energy (-212.0 kJ mol^{-1}). In contrast, no accessible oxygen bridge species are close to $\mathbf{G_{4ax/eq}}$, thus water dissociation does not take place and the adsorption energy per water molecule is significantly lower (-155.7 kJ mol^{-1}).

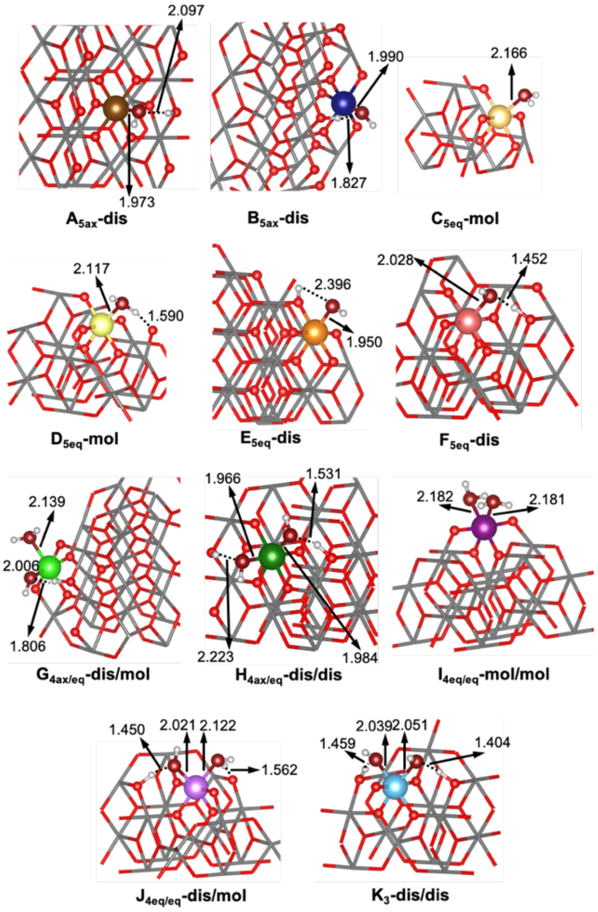

Figure 4. Optimized structure for the most favorable water adsorption form at the different $(IrO_2)_{115}$ nanoparticle sites. See Figure 1 for labelling. Distances are in Å

The same reasoning can be applied to the sites presenting only equatorial vacancies. Four different pentacoordinated sites with an equatorial vacant site can be distinguished in $(IrO_2)_{115}$: $\mathbf{C_{5eq}}$, $\mathbf{D_{5eq}}$, $\mathbf{E_{5eq}}$ and $\mathbf{F_{5eq}}$. The adsorption energy in these sites ranges between -183.3 and -111.9 kJ mol^{-1}, the highest value being obtained at $\mathbf{F_{5eq}}$ which is located on the (011) surface and it presents a well-placed oxygen bridge for stablishing a strong hydrogen bond that reinforces the H_2O-nanoparticle interaction and favor water dissociation. On the other hand, $\mathbf{C_{5eq}}$, $\mathbf{D_{5eq}}$ and $\mathbf{E_{5eq}}$ are located at edges or corners between different surfaces and the morphology around these sites is more convex. Consequently, no strong hydrogen bonds can be stablished, which leads to smaller adsorption energies and tend to favor the **mol** form. Similarly, the two tetracoordinated sites with equatorial vacancies ($\mathbf{I_{4eq/eq}}$ and $\mathbf{J_{4eq/eq}}$) present different preferred forms that can be related with the accessibility to oxygen bridge sites. $\mathbf{I_{4eq/eq}}$ is located at the tip of the nanoparticle and the convex form around this site prevents the formation of any hydrogen bond. Consequently, the adsorption energy is low (-113.8 kJ mol^{-1}) and the **mol/mol** form preferred.

$J_{4eq/eq}$ is located at the edge between two {011} surfaces and the morphology around the site allows stablishing one hydrogen bond per water molecule. This results in a higher adsorption energy (-182.6 kJ mol^{-1}) and the preference for the **mol/dis** form. Indeed, geometry optimizations starting from a **mol/mol** and a **dis/dis** structure, spontaneously evolved to the **mol/dis** one.

In summary results for the larger nanoparticle indicate that the main conclusions already drawn with the small nanoparticle model are also valid for the larger one. Indeed, the vacant site nature determines in a large extend the preferred adsorption form at low coverages: **dis** for axial vacant sites and a competition between the two forms in the equatorial one. Indeed, when no strong hydrogen bonds are stablished between the adsorbed water and the oxygen bridge of the nanoparticle, the preferred structure in equatorial sites is the **mol** form. In contrast, the presence of strong hydrogen bonds favors the **dis** form that becomes more favorable. Moreover, the adsorption energy is highly determined by the feasibility to stablish hydrogen bonding between the adsorbed species and the nanoparticle. Therefore, within centers with the same type of vacant site the adsorption energy varies as face > edge > corners = tips. This is somewhat counter-intuitive, since the most accessible sites present lower adsorption energies, but outlines the importance of hydrogen bonding in the interaction between water and IrO_2. Finally, the two nanoparticle models seem to show a larger ionicity than the extended surfaces, thus leading to stronger intrinsic Ir-H_2O interactions. However, the IrO_2 ionicity appears to slightly decrease when enlarging the nanoparticle model, leading to a small decrease of the adsorption energy at equivalent sites of the two nanoparticle models.

Cooperative and thermal effects: AIMD simulations of the $(IrO_2)_{33}$ monolayer.

Interaction between different adsorbed water molecules is expected to influence the IrO_2 nanoparticle - H_2O interaction as already described on the IrO_2 (110) and (011) surfaces.[35] It is for this reason that we explored the formation of a water monolayer around the $(IrO_2)_{33}$ nanoparticle model. This implies 38 water molecules that occupies all iridium vacant sites. Since many different structures are plausible, we decided to optimize two limit situations: a) all adsorbed molecules are in their **mol** form and b) a structure with the maximum number of dissociated water molecules (28 **dis**/10 **mol**), which is limited by the accessible oxygen dangling and oxygen bridge sites. In a second step, we performed a 10 ps AIMD simulation starting from the two optimized structures.

The two $(IrO_2)_{33}$-monolayer optimized structures show the 38 water molecules interacting with iridium thus, the water coverage increase does not produce any water desorption (Figure S8). However, the resulting structure differs from the initial one in the two cases. The geometry optimization starting from a monolayer composed of adsorbed molecular water evolves spontaneously to a situation where half of the water molecules dissociate (19 **dis**/19 **mol**) and this is linked with the protonation of 5 of the 6 dangling oxygens. On the other hand, the optimization starting from the maximum number of dissociated water molecules also implies proton transfer, the final structure presenting 27 **dis**/11 **mol** water molecules and all dangling oxygens protonated. In both cases, an important network of hydrogen bonding between the adsorbed species is stablished except for some species at the equatorial position of **C_{5eq}** and **$G_{4ax/eq}$** (Figure S8). Moreover, there is an elongation of the Ir-O_W average distance (2.09 Å and 2.05 Å for the 19 **dis**/19 **mol** and 27 **dis**/11 **mol** structures respectively) when compared with the isolated adsorption of one water molecule (2.02 Å). Therefore, cooperative effects between water molecules decrease the H_2O-IrO_2 nanoparticle interaction. Remarkably, the adsorption energy per water molecule for the two final conformations (-172.1 and -176.0 kJ mol^{-1} for 19 **dis**/19 **mol** and 27 **dis**/11 **mol** structures respectively) is very similar to the average value considering the individual adsorption in each site, -178.2 kJ mol^{-1}. That is, the cooperative effects compensate the loss of local H_2O-IrO_2 interaction but does not imply a significant increase of the adsorption energy. This was already found for the (110) surface and it is in contrast to the results for the (011) IrO_2 surface.[35]

Since the difference in adsorption energy per water molecule in the two limit cases is small, they are both expected to contribute to the water-monolayer structure. Indeed, other relevant conformations may be close in energy and contribute to the final interface structure. Moreover, thermal effects are expected to play a role as evidenced by AIMD simulations on the (110) and (011) surfaces of RuO_2, IrO_2 and TiO_2, which show that cooperative and temperature effects tend to disfavor water dissociation, particularly on IrO_2.[35] It is for this reason that 10ps AIMD simulations starting from the two limit situations were carried out. Analysis of the degree of dissociation along time (Figure S9) shows that equilibration last up to 5ps, thus the analysis is made on the 5 to 10ps steps. Figure 5 shows the frequency of different number of water molecules on the nanoparticle (including those formed on dangling oxygens) and how they are divided in axial and equatorial sites and reports the mean degree of dissociation for the whole nanoparticle and as function of each type of sites.

During the equilibration period, the AIMD simulation starting from the optimized structure with a larger number of molecular waters evolve to a structure with a higher water dissociation degree. In contrast, the opposite process is observed during the equilibration period of the AIMD starting from the optimized structure with many dissociated water molecules. The average number of H_2O species during the production period are 16.8 and 11.4 for the simulation starting with more **mol** or **dis** water molecules, respectively. Detailed analysis (Figure S10) shows that the differences can be attributed in a large extend to **C_{5eq}** and **$I_{4eq/4eq}$** sites, where the hydrogen bonding network between adsorbed water molecules is weaker and the energy difference between **mol** and **dis** forms small. The degree of water dissociation (63%; average value considering the two simulations) is higher for those water molecules adsorbed at axial sites (around 72 %) than those adsorbed at equatorial sites

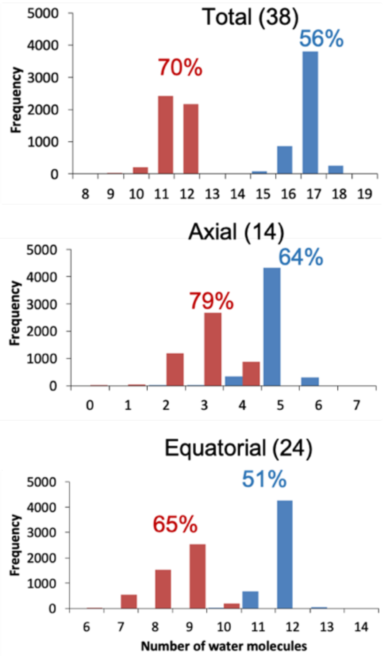

Figure 5. Frequency of the different number of water molecules and the percentage of water dissociation on the nanoparticle surface. The total number of water molecules is divided as axial and equatorial. Bars and values in blue correspond to the AIMD simulation with a larger fraction of molecular waters, while the bars and values in red correspond to the simulation starting from a large degree of dissociation.

(58 %) and these values are similar albeit marginally lower than those arising from the study of individual adsorptions (68 %).

In summary, the presence of stabilizing cooperative effects between adsorbed water molecules and thermal contributions weakens the IrO_2-H_2O direct interaction. This produces a decrease of the water dissociation degree (around 63%) that is tuned by two additional factors: i) cooperative effects and ii) the number of accessible oxygen bridge and dangling atoms is smaller than the number of adsorbed water molecules. The latter seems to be dominant and, thus overall, the degree of dissociation is lower than those of films.

Conclusions

Periodic PBE-D2 calculations and AIMD simulations have been carried out to study the interface between H_2O and Wulff-like stoichiometric IrO_2 nanoparticles. For that, different coverages ranging from isolated water molecules to the monolayer as well as two nanoparticle models ($(IrO_2)_{33}$ and $(IrO_2)_{115}$) constructed with BCN-M have been considered.[43] Results show that the adsorption energies range from -232.6 and -111.9 kJ mol^{-1} and these values are similar (upper limit) or lower than those obtained in extended surfaces. The tetragonal distortion present on IrO_2 rutile bulk is retained on the nanoparticle models and this controls the adsorption strength and the preferred structure (molecular (**mol**) or dissociated (**dis**)) at each site. H_2O adsorption on axial vacant sites is strong, favoring water dissociation, which is largely preferred. The H_2O-Ir interaction at equatorial vacant sites is weaker and the **mol** and **dis** forms become close in energy. In these equatorial sites, the **dis** form is preferred when strong hydrogen bonding is stablished with a nearby oxygen bridge atom. However, nanoparticle morphology around corner and tip sites prevents the formation of hydrogen bonds and thus, the **mol** form becomes predominant in the more convex regions of the nanoparticle. The hydrogen bonding also influences in a large extent the final adsorption energy. Consequently, the highest adsorption energies are obtained at face and edge sites with a flat morphology, and the smallest values are related to corners and tips. That is, the usually less stabilized and more accessible sites present weaker adsorption energies due to the absence of hydrogen bonding.

Increasing water coverage from an isolated water to a water monolayer reveals that cooperative effects weaken the IrO_2-H_2O interaction, which is essentially compensated by the hydrogen bonding between adsorbed species. Furthermore, the global water dissociation degree is highly determined by the accessible unsaturated oxygen atoms on the nanoparticle surface that are not sufficient to account for all the potential dissociations. Overall, the water dissociation degree is between 60 and 70%, which is lower than that obtained for crystalline surfaces. This is in line with the observation that nanoparticles with large amounts of surface Ir-OH species are highly amorph and this is related to their higher activity in OER.[16]

Authors contribution

DG performed all simulations of the present contribution. MS, LRS and XSM conceived the project, supervised the research and wrote the paper.

Conflicts of interest

There are no conflicts to declare

Acknowledgements

The authors gratefully acknowledge financial support from MICINN [CTQ2017-89132-P and PID2020-112715GB-I00], the Generalitat de Catalunya [2017SGR1323] and Red Española de Supercomputación [QCM-2019-1-0043, QS-2019-2-0031]. XSM is grateful for the Professor Agregat Serra Húnter position.

References

1 Z. W. Seh, J. Kibsgaard, C. F. Dickens, I. Chorkendorff, J. K. Nørskov and T. F. Jaramillo, *Science*, 2017, **355**, eaad4998.
2 C. C. L. McCrory, S. Jung, I. M. Ferrer, S. M. Chatman, J. C. Peters and T. F. Jaramillo, *J. Am. Chem. Soc.*, 2015, **137**, 4347–4357.
3 T. Reier, H. N. Nong, D. Teschner, R. Schlögl and P. Strasser, *Adv. Energy Mater.*, 2017, **7**, 1601275.
4 J. H. Montoya, L. C. Seitz, P. Chakthranont, A. Vojvodic, T. F. Jaramillo and J. K. Nørskov, *Nat. Mater.*, 2017, **16**, 70–81.
5 O. Piqué, F. Illas and F. Calle-Vallejo, *Phys. Chem. Chem. Phys.*, 2020, **22**, 6797–6803.
6 J. Rossmeisl, Z.-W. Qu, H. Zhu, G.-J. Kroes and J. K. Nørskov,

J. Electroanal. Chem., 2007, **607**, 83–89.

7 H. N. Nong, L. J. Falling, A. Bergmann, M. Klingenhof, H. P. Tran, C. Spöri, R. Mom, J. Timoshenko, G. Zichittella, A. Knop-Gericke, S. Piccinin, J. Pérez-Ramírez, B. R. Cuenya, R. Schlögl, P. Strasser, D. Teschner and T. E. Jones, *Nature*, 2020, **587**, 408–413.

8 Y. Bian, M. Kim, T. Li, A. Asthagiri and J. F. Weaver, *J. Am. Chem. Soc.*, 2018, **140**, 2665–2672.

9 Y. Tsuji and K. Yoshizawa, *J. Phys. Chem. C*, 2018, **122**, 15359–15381.

10 Z. Liang, T. Li, M. Kim, A. Asthagiri and J. F. Weaver, *Science*, 2017, **356**, 299–303.

11 H.-S. Oh, H. N. Nong, T. Reier, A. Bergmann, M. Gliech, J. Ferreira de Araújo, E. Willinger, R. Schlögl, D. Teschner and P. Strasser, *J. Am. Chem. Soc.*, 2016, **138**, 12552–12563.

12 T. Audichon, T. W. Napporn, C. Canaff, C. Morais, C. Comminges and K. B. Kokoh, *J. Phys. Chem. C*, 2016, **120**, 2562–2573.

13 L. An, C. Wei, M. Lu, H. Liu, Y. Chen, G. G. Scherer, A. C. Fisher, P. Xi, Z. J. Xu and C. Yan, *Adv. Mater.*, 2021, **33**, 2006328.

14 H. N. Nong, T. Reier, H.-S. Oh, M. Gliech, P. Paciok, T. H. T. Vu, D. Teschner, M. Heggen, V. Petkov, R. Schlögl, T. Jones and P. Strasser, *Nat. Catal.*, 2018, **1**, 841–851.

15 D. Lebedev, R. Ezhov, J. Heras-Domingo, A. Comas-Vives, N. Kaeffer, M. Willinger, X. Solans-Monfort, X. Huang, Y. Pushkar and C. Copéret, *ACS Cent. Sci.*, 2020, **6**, 1189–1198.

16 D. F. Abbott, D. Lebedev, K. Waltar, M. Povia, M. Nachtegaal, E. Fabbri, C. Copéret and T. J. Schmidt, *Chem. Mater.*, 2016, **28**, 6591–6604.

17 A. W. Jensen, G. W. Sievers, K. D. Jensen, J. Quinson, J. A. Arminio-Ravelo, V. Brüser, M. Arenz and M. Escudero-Escribano, *J. Mater. Chem. A*, 2020, **8**, 1066–1071.

18 E. Oakton, D. Lebedev, M. Povia, D. F. Abbott, E. Fabbri, A. Fedorov, M. Nachtegaal, C. Copéret and T. J. Schmidt, *ACS Catal.*, 2017, **7**, 2346–2352.

19 P. Lettenmeier, L. Wang, U. Golla-Schindler, P. Gazdzicki, N. A. Cañas, M. Handl, R. Hiesgen, S. S. Hosseiny, A. S. Gago and K. A. Friedrich, *Angew. Chemie Int. Ed.*, 2016, **55**, 742–746.

20 F. Bizzotto, J. Quinson, A. Zana, J. J. K. Kirkensgaard, A. Dworzak, M. Oezaslan and M. Arenz, *Catal. Sci. Technol.*, 2019, **9**, 6345–6356.

21 Y. Lee, J. Suntivich, K. J. May, E. E. Perry and Y. Shao-Horn, *J. Phys. Chem. Lett.*, 2012, **3**, 399–404.

22 Y. Zhao, E. A. Hernandez-Pagan, N. M. Vargas-Barbosa, J. L. Dysart and T. E. Mallouk, *J. Phys. Chem. Lett.*, 2011, **2**, 402–406.

23 D. Lebedev and C. Copéret, *ACS Appl. Energy Mater.*, 2019, **2**, 196–200.

24 H. Jiang, S. Ge, Y. Zhang, M. Dong, S. Wu, M. Wu, J. Zhang, R. Ge and Z. Guo, *J. Phys. Chem. C*, 2020, **124**, 2–8.

25 L. Fu, X. Zeng, C. Huang, P. Cai, G. Cheng and W. Luo, *Inorg. Chem. Front.*, 2018, **5**, 1121–1125.

26 D. Böhm, M. Beetz, M. Schuster, K. Peters, A. G. Hufnagel, M. Döblinger, B. Böller, T. Bein and D. Fattakhova-Rohlfing, *Adv. Funct. Mater.*, 2020, **30**, 1906670.

27 M. Kan, X. Qian, T. Zhang, D. Yue and Y. Zhao, *ACS Sustain. Chem. Eng.*, 2017, **5**, 10940–10946.

28 F. A. Frame, T. K. Townsend, R. L. Chamousis, E. M. Sabio, T. Dittrich, N. D. Browning and F. E. Osterloh, *J. Am. Chem. Soc.*, 2011, **133**, 7264–7267.

29 J. C. Cruz, V. Baglio, S. Siracusano, R. Ornelas, L. Ortiz-Frade, L. G. Arriaga, V. Antonucci and A. S. Aricò, *J. Nanoparticle Res.*, 2011, **13**, 1639–1646.

30 R. Zhang, P. E. Pearce, Y. Duan, N. Dubouis, T. Marchandier and A. Grimaud, *Chem. Mater.*, 2019, **31**, 8248–8259.

31 R. Jaimes, J. Vazquez-Arenas, I. González and M. Galván, *Electrochim. Acta*, 2017, **229**, 345–351.

32 D.-Y. Kuo, J. K. Kawasaki, J. N. Nelson, J. Kloppenburg, G. Hautier, K. M. Shen, D. G. Schlom and J. Suntivich, *J. Am. Chem. Soc.*, 2017, **139**, 3473–3479.

33 S. Siahrostami and A. Vojvodic, *J. Phys. Chem. C*, 2015, **119**, 1032–1037.

34 J. Heras-Domingo, M. Sodupe and X. Solans-Monfort, *J. Phys. Chem. C*, 2019, **123**, 7786–7798.

35 D. González, J. Heras-Domingo, S. Pantaleone, A. Rimola, L. Rodríguez-Santiago, X. Solans-Monfort and M. Sodupe, *ACS Omega*, 2019, **4**, 2989–2999.

36 R. R. Rao, M. J. Kolb, J. Hwang, A. F. Pedersen, A. Mehta, H. You, K. A. Stoerzinger, Z. Feng, H. Zhou, H. Bluhm, L. Giordano, I. E. L. Stephens and Y. Shao-Horn, *J. Phys. Chem. C*, 2018, **122**, 17802–17811.

37 L. Mino, Á. Morales-García, S. T. Bromley and F. Illas, *Nanoscale*, 2021, **13**, 6577–6585.

38 G. Fazio, D. Selli, L. Ferraro, G. Seifert and C. Di Valentin, *ACS Appl. Mater. Interfaces*, 2018, **10**, 29943–29953.

39 D. R. Hummer, J. D. Kubicki, P. R. C. Kent and P. J. Heaney, *J. Phys. Chem. C*, 2013, **117**, 26084–26090.

40 A. Cuko, A. Macià Escatllar, M. Calatayud and S. T. Bromley, *Nanoscale*, 2018, **10**, 21518–21532.

41 F. A. Soria and C. Di Valentin, *Nanoscale*, 2021, **13**, 4151–4166.

42 D. González, J. Heras-Domingo, M. Sodupe, L. Rodríguez-Santiago and X. Solans-Monfort, *J. Catal.*, 2021, **396**, 192–201.

43 D. González, B. Camino, J. Heras-Domingo, A. Rimola, L. Rodríguez-Santiago, X. Solans-Monfort and M. Sodupe, *J. Phys. Chem. C*, 2020, **124**, 1227–1237.

44 G. Kresse and J. Furthmüller, *Phys. Rev. B*, 1996, **54**, 11169–11186.

45 G. Kresse and J. Hafner, *Phys. Rev. B*, 1993, **47**, 558–561.

46 J. P. Perdew, K. Burke and M. Ernzerhof, *Phys. Rev. Lett.*, 1996, **77**, 3865–3868.

47 S. Grimme, *J. Comput. Chem.*, 2004, **25**, 1463–1473.

48 G. Kresse and D. Joubert, *Phys. Rev. B*, 1999, **59**, 1758–1775.

49 P. E. Blöchl, *Phys. Rev. B*, 1994, **50**, 17953–17979.

50 A. Minguzzi, O. Lugaresi, E. Achilli, C. Locatelli, A. Vertova, P. Ghigna and S. Rondinini, *Chem. Sci.*, 2014, **5**, 3591.

51 C. F. Dickens, J. H. Montoya, A. R. Kulkarni, M. Bajdich and J. K. Nørskov, *Surf. Sci.*, 2019, **681**, 122–129.

52 B. Hammer and J. K. Nørskov, *Surf. Sci.*, 1995, **343**, 211–

220.

53 Z. Xu and J. R. Kitchin, *Catal. Commun.*, 2014, **52**, 60–64.